IEEE Access
Multidisciplinary | Rapid Review | Open Access Journal

Received May 12, 2021, accepted May 25, 2021, date of publication June 7, 2021, date of current version June 17, 2021.

Digital Object Identifier 10.1109/ACCESS.2021.3086769

A Combined Mode-Matching Technique and Born Approximation Method to Model Well-Logging Sensors in Non-Axisymmetric Boreholes

LISSETH SAAVEDRA, (Member, IEEE), GUILHERME S. ROSA, (Member, IEEE), AND JOSÉ R. BERGMANN, (Life Senior Member, IEEE)
Centre for Telecommunications Studies, Pontifical Catholic University of Rio de Janeiro, Rio de Janeiro 22451-900, Brazil

Corresponding author: Lisseth Saavedra (lissethsaavedra@cetuc.puc-rio.br)

This work was supported in part by the Coordenação de Aperfeiçoamento de Pessoal de Nível Superior—Brasil (CAPES) under Finance Code 001, and in part by the Brazilian Agency Conselho Nacional de Desenvolvimento Científico e Tecnológico (CNPq) under Grant 140797/2016-5.

ABSTRACT This paper presents a study on pseudo-analytic techniques for modeling electromagnetic sensors used in geophysical well logging. Logging-while-drilling (LWD) tools are sensors typically used on the exploration of hydrocarbons reservoirs and are usually immersed in complex geophysical formations (inhomogeneous, dissipative, and anisotropic), resulting in a challenging problem for conventional computational electromagnetic techniques. The geophysical environment is typically treated as a radially and longitudinally stratified medium, conforming with the boundaries of a cylindrical borehole drilled in the earth. We analyzed this propagation problem by using a full-wave method based on the mode-matching technique for solving the cylindrical stratifications. This method was then supplemented by a perturbational solution on the grounds of the Born approximation for handling the non-symmetries the borehole and earth layers can present. Preliminary results show the ability of the techniques introduced in this paper to accurately modeling electromagnetic sensors more realistically when compared with other semi-analytic methods available in the literature.

INDEX TERMS Born-based approximation, mode-matching techniques, full-wave techniques, scattering, well-logging sensors.

I. INTRODUCTION

Electromagnetic (EM) logging-while-drilling (LWD) tools are sensors that provide geophysical formation data for guiding the identification of hydrocarbon reservoirs [1], [2] during the process of drilling a borehole in the earth. In particular, low-frequency electromagnetic LWD sensors can be used for characterizing the apparent resistivity profile in the vicinity of a borehole, allowing to identifying the constitutive parameters of the earth, and enabling a real-time well placement toward potential pay-zones. A LWD tool usually comprises an array of solenoid loop antennas wounded on the drilling mandrel [1]–[6]. In the simplified scenario depicted in Fig. 1, the transmitting antenna (TX) induces an electromotive force (voltage) at the receiving (RX) one, and the amplitude and phase voltage at RX can then be used into inverse algorithms to calculate the earth resistivity [7]–[10]. The induced voltage at the receiver is dramatically affected by the geophysical environment where the antennas are immersed, which can present anisotropic characteristics [11].

The geometry of the formation can be approximated as a vertically layered medium [12]–[14] for determining the environmental effects, and by a radially layered medium [7], [15]–[17] for accounting the effects of the borehole and other radial layers. Mode-matching-based techniques are typically employed to account for inhomogeneities in both radial and axial directions of symmetric boreholes. A mature and extensively studied implementation is the numerical mode-matching (NMM) technique that combines a 1D finite-element method in one coordinate direction with a field matching in the transversal direction. The NMM has been extensively used for modeling LWD applications [18]–[22].

The associate editor coordinating the review of this manuscript and approving it for publication was Yilun Shang.

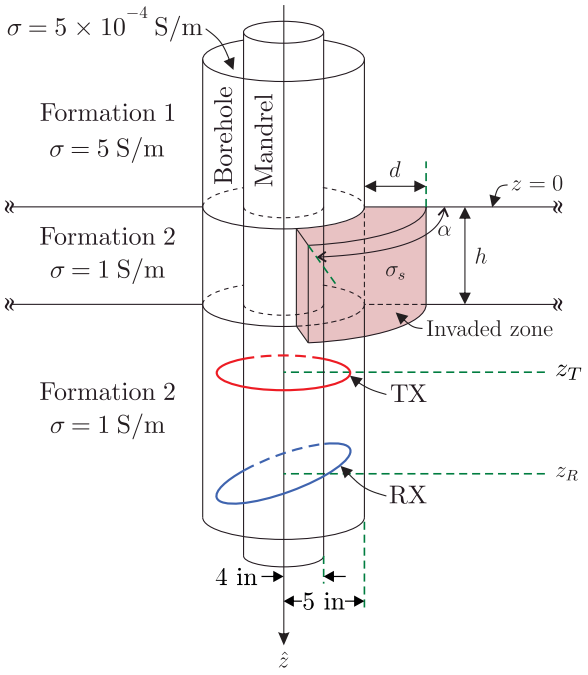

FIGURE 1. Asymmetric invasion zone on a layered cylindrical medium.

Alternatively, the mode-matching solution presented in [7], [16] does not rely on spatial discretization as the former method, and, analytical results for the required coupling integrals are available.

Besides the ability to deal with cylindrical-conforming boreholes, such approaches cannot properly model underground prospecting scenarios where a non-axisymmetric object is present, disturbing the LWD tool response. For example, consider the idealized mud-invaded zone depicted in Fig. 1. Realistic scattering objects could be an injection well drilled parallel to the main production line, a hydraulic fracture in the formation, a tilted bed layer, among others [11], [14], [23], [24].

Integral equation-based methods are widely used for modeling the scattering by arbitrarily shaped objects because of their flexibility in handling irregular boundaries [25]–[29]. These brute-force methods require the computation and the inversion of a large complex matrix, whose computational cost can become prohibitive in multi-scale EM problems as those will be discussed in this paper. Motivated to overcome these issues, we have investigated semi-analytic methods that can provide a reduction in the computational effort required to modeling realistic LWD sensors. We propose herein an alternative method for modeling the field perturbation due to a three-dimensional (3D), lossy, and anisotropic scatterer inside a cylindrically layered medium, as illustrated in Fig. 1.

Our approach comprises two steps: first, we solve the electromagnetic problem in the absence of the non-symmetric object by using the mode-matching-based method presented in [7], [16]. Then, the field perturbation due to the scatterer is calculated using the Born approximation (BA) [18, Sec. 8.10.1].

The BA requires the dyadic Green's functions (DGFs) for representing the media, and getting these is not a trivial task for an inhomogeneous background. For this reason, several works have addressed the problem by using the DGFs for homogeneous and isotropic background media [18], [30]–[32], and the layered background, as well as the non-axisymmetric scattering objects, is then evaluated via volumetric integrals throughout the entire simulation domain. As an example, for modeling the borehole drilled into the ground depicted in Fig. 1, assuming the background as the formation in 1, this approach requires the computation of volume integrals over a) the metallic cylindrical mandrel, b) the borehole, c) the formation 2, and d) the invaded zone. The novelty of this work is the employment of pseudo-analytic[1] DGFs for inhomogeneous (cylindrically layered with vertical and horizontal layers) media as a basis for the BA algorithm. Our strategy only requires the computation of a volumetric integral over the invaded (irregular) zone. The work in [14] has employed a strategy similar to that proposed here, on decomposing the problem into regular and irregular regions. However, this former work does not consider anisotropic and magnetic scatterers as the method shown here.

We organize the rest of this paper as follows. In Section II, we present a brief electromagnetic description of the perturbation BA method for modeling non-symmetric objects immersed in cylindrical-stratified media. We present a novel formulation for the DGFs of a cylindrically stratified medium composed of vertical and horizontal layers on the basis of the mode-matching technique (MMT). In Section III several numerical examples are explored for evidencing the impact of borehole perturbations on the induced voltage at the LWD sensor. The proposed perturbation method can model small objects surrounding a logging well or scatterers with a weak contrast referring to the background medium. This method can provide useful approximations for modeling the effect of deformed (no-circular) boreholes and small-angle dipping beds on the LWD sensor response. Finally, concluding remarks are presented in Section IV.

II. FORMULATION

The non-axisymmetric geometry shown in Fig. 1 is used to model the geophysical formation where the logging sensor is immersed. In this model, the formation comprises a cylindrical axially and radially layered medium perturbed by a small inhomogeneous scatterer. We assume the source (TX antenna) is fed by a sinusoidal time-harmonic current. In the frequency domain, we assume the $\exp(-i\omega t)$ convention, and the complex permeability $\bar{\bar{\mu}}(\mathbf{r})$ and permittivity $\bar{\bar{\epsilon}}(\mathbf{r})$ tensors are assumed functions of the position $\mathbf{r}$.

[1] In this work, the terms 'pseudo-analytic' and 'semi-analytic' are used to distinguish the present approach from the so-called brute-force techniques, such as finite elements, finite differences, finite integration, and method of moments.

A. ELECTROMAGNETIC FIELD SCATTERED BY ANISOTROPIC OBJECT

Adopting a notation similar to that in [18], [33], the Maxwell's equations in an anisotropic media can be used to derive the vector wave equations

$$\nabla \times \bar{\bar{\mu}}^{-1}(\mathbf{r}) \cdot \nabla \times \mathbf{E}(\mathbf{r}) - \omega^2 \bar{\bar{\epsilon}}(\mathbf{r}) \cdot \mathbf{E}(\mathbf{r}) = i\omega \mathbf{J}(\mathbf{r}) - \nabla \times \bar{\bar{\mu}}^{-1}(\mathbf{r}) \cdot \mathbf{M}(\mathbf{r}), \quad (1)$$

$$\nabla \times \bar{\bar{\epsilon}}^{-1}(\mathbf{r}) \cdot \nabla \times \mathbf{H}(\mathbf{r}) - \omega^2 \bar{\bar{\mu}}(\mathbf{r}) \cdot \mathbf{H}(\mathbf{r}) = i\omega \mathbf{M}(\mathbf{r}) + \nabla \times \bar{\bar{\epsilon}}^{-1}(\mathbf{r}) \cdot \mathbf{J}(\mathbf{r}). \quad (2)$$

Dyadic Green's functions can be used to relate the vector electric and magnetic fields to the electric and magnetic current densities via

$$\mathbf{E}(\mathbf{r}) = \int_V \bar{\bar{G}}^{ee}(\mathbf{r}, \mathbf{r}') \cdot \mathbf{J}(\mathbf{r}')\, d\mathbf{r}' + \int_V \bar{\bar{G}}^{eh}(\mathbf{r}, \mathbf{r}') \cdot \mathbf{M}(\mathbf{r}')\, d\mathbf{r}', \quad (3)$$

$$\mathbf{H}(\mathbf{r}) = \int_V \bar{\bar{G}}^{he}(\mathbf{r}, \mathbf{r}') \cdot \mathbf{J}(\mathbf{r}')\, d\mathbf{r}' + \int_V \bar{\bar{G}}^{hh}(\mathbf{r}, \mathbf{r}') \cdot \mathbf{M}(\mathbf{r}')\, d\mathbf{r}', \quad (4)$$

where $\bar{\bar{G}}^{ee}$ is the electric DGF due to an impulsive spatial electric current excitation. All other remaining DGFs are defined according to their superscripts: the first one defines the field (electric e or magnetic h), and the second defines the kind of excitation current (electric e or magnetic h).

We divide the geophysical medium into two sub-domains: the earth formation and the scattering object. The earth, also denoted here as background, is composed of cylindrical conforming layers and characterized by the constitutive parameters $\bar{\bar{\epsilon}}_b(\mathbf{r})$ and $\bar{\bar{\mu}}_b(\mathbf{r})$.

We can write the constitutive tensors at any point of the geophysical formation as

$$\bar{\bar{\epsilon}}(\mathbf{r}) = \bar{\bar{\epsilon}}_b(\mathbf{r}) + \Delta\bar{\bar{\epsilon}}(\mathbf{r}), \quad (5)$$

$$\bar{\bar{\mu}}(\mathbf{r}) = \bar{\bar{\mu}}_b(\mathbf{r}) + \Delta\bar{\bar{\mu}}(\mathbf{r}), \quad (6)$$

where $\Delta\bar{\bar{\epsilon}}(\mathbf{r})$ and $\Delta\bar{\bar{\mu}}(\mathbf{r})$ describe the permittivity and permeability variations inside the scatterer regarding the background medium, respectively.

The electromagnetic fields of the background, namely, $\mathbf{E}_b(\mathbf{r})$ and $\mathbf{H}_b(\mathbf{r})$, can be properly solved by using the semi-analytic method presented in [7]. The perturbation fields due to the scatterer, namely, $\mathbf{E}_s(\mathbf{r})$ and $\mathbf{H}_s(\mathbf{r})$, can then be evaluated by employing the induction theorem [34, p. 113–116], and thereby the total fields can be computed via

$$\mathbf{E}(\mathbf{r}) = \mathbf{E}_b(\mathbf{r}) + \mathbf{E}_s(\mathbf{r}), \quad (7)$$

$$\mathbf{H}(\mathbf{r}) = \mathbf{H}_b(\mathbf{r}) + \mathbf{H}_s(\mathbf{r}). \quad (8)$$

In view of (3) and (4), the background and scattered fields are given by

$$\mathbf{E}_b(\mathbf{r}) = \int_V \bar{\bar{G}}^{ee}(\mathbf{r}, \mathbf{r}') \cdot \mathbf{J}_i(\mathbf{r}')\, d\mathbf{r}' + \int_V \bar{\bar{G}}^{eh}(\mathbf{r}, \mathbf{r}') \cdot \mathbf{M}_i(\mathbf{r}')\, d\mathbf{r}', \quad (9)$$

$$\mathbf{H}_b(\mathbf{r}) = \int_V \bar{\bar{G}}^{he}(\mathbf{r}, \mathbf{r}') \cdot \mathbf{J}_i(\mathbf{r}')\, d\mathbf{r}' + \int_V \bar{\bar{G}}^{hh}(\mathbf{r}, \mathbf{r}') \cdot \mathbf{M}_i(\mathbf{r}')\, d\mathbf{r}', \quad (10)$$

and

$$\mathbf{E}_s(\mathbf{r}) = -i\omega \int_V \bar{\bar{G}}^{ee}(\mathbf{r}, \mathbf{r}_0) \cdot \Delta\bar{\bar{\epsilon}}(\mathbf{r}_0) \cdot \mathbf{E}(\mathbf{r}_0)\, d\mathbf{r}_0 - i\omega \int_V \bar{\bar{G}}^{eh}(\mathbf{r}, \mathbf{r}_0) \cdot \Delta\bar{\bar{\mu}}(\mathbf{r}_0) \cdot \mathbf{H}(\mathbf{r}_0)\, d\mathbf{r}_0, \quad (11)$$

$$\mathbf{H}_s(\mathbf{r}) = -i\omega \int_V \bar{\bar{G}}^{he}(\mathbf{r}, \mathbf{r}_0) \cdot \Delta\bar{\bar{\epsilon}}(\mathbf{r}_0) \cdot \mathbf{E}(\mathbf{r}_0)\, d\mathbf{r}_0 - i\omega \int_V \bar{\bar{G}}^{hh}(\mathbf{r}, \mathbf{r}_0) \cdot \Delta\bar{\bar{\mu}}(\mathbf{r}_0) \cdot \mathbf{H}(\mathbf{r}_0)\, d\mathbf{r}_0. \quad (12)$$

In the above, the TX antenna contributes with the impressed electric and magnetic current densities $\mathbf{J}_i(\mathbf{r})$ and $\mathbf{M}_i(\mathbf{r})$, respectively. The scattering object contributes with the equivalent electric and magnetic current densities $\mathbf{J}_s(\mathbf{r}) = -i\omega\Delta\bar{\bar{\epsilon}}(\mathbf{r}) \cdot \mathbf{E}(\mathbf{r})$ and $\mathbf{M}_s(\mathbf{r}) = -i\omega\Delta\bar{\bar{\mu}}(\mathbf{r}) \cdot \mathbf{H}(\mathbf{r})$, respectively. Also, position vectors $\mathbf{r}'$ and $\mathbf{r}_0$ are used to describe the TX source and the scatterer object, respectively.

B. BORN APPROXIMATION

According to the BA theory [25], [30], [31], [35], if the scatterer is small when compared with the working wavelength, the fields on the scatterer can be approximated by the background counterparts, i.e.,

$$\mathbf{E}(\mathbf{r}_0) \approx \mathbf{E}_b(\mathbf{r}_0), \quad (13)$$

$$\mathbf{H}(\mathbf{r}_0) \approx \mathbf{H}_b(\mathbf{r}_0), \quad (14)$$

for $\mathbf{r} - \mathbf{r}_0 \approx \mathbf{0}$. Consequently, the total fields in (7) and (8) become

$$\mathbf{E}(\mathbf{r}) \approx \mathbf{E}_b(\mathbf{r}) - i\omega \int_V \bar{\bar{G}}^{ee}(\mathbf{r}, \mathbf{r}_0) \cdot \Delta\bar{\bar{\epsilon}}(\mathbf{r}_0) \cdot \mathbf{E}_b(\mathbf{r}_0)\, d\mathbf{r}_0 - i\omega \int_V \bar{\bar{G}}^{eh}(\mathbf{r}, \mathbf{r}_0) \cdot \Delta\bar{\bar{\mu}}(\mathbf{r}_0) \cdot \mathbf{H}_b(\mathbf{r}_0)\, d\mathbf{r}_0, \quad (15)$$

$$\mathbf{H}(\mathbf{r}) \approx \mathbf{H}_b(\mathbf{r}) - i\omega \int_V \bar{\bar{G}}^{he}(\mathbf{r}, \mathbf{r}_0) \cdot \Delta\bar{\bar{\epsilon}}(\mathbf{r}_0) \cdot \mathbf{E}_b(\mathbf{r}_0)\, d\mathbf{r}_0 - i\omega \int_V \bar{\bar{G}}^{hh}(\mathbf{r}, \mathbf{r}_0) \cdot \Delta\bar{\bar{\mu}}(\mathbf{r}_0) \cdot \mathbf{H}_b(\mathbf{r}_0)\, d\mathbf{r}_0. \quad (16)$$

Higher-order approximations to (13) and (14) can be obtained using the so-called extended Born approximation (EBA), but with severe impairments of the computational cost when compared with the standard BA. For further details on the EBA, please see [25], [30]–[32] and [35].

C. COMPUTATION OF THE DYADIC GREEN'S FUNCTIONS

Calculating the fields will require computing the DGFs of the background media. We propose to use a modal field solution in a stratified cylindrical medium, with both radial and axial stratifications as a basis for the calculation of the DGFs. Initially, we will establish the mathematical formalism for the electric dyadic $\bar{\bar{G}}^{ee}(\mathbf{r}, \mathbf{r}_0)$, then it will be generalized for the

other dyadic functions. We can express the electric dyadic in cylindrical coordinates as

$$\bar{\bar{G}}^{ee}(\mathbf{r}, \mathbf{r}_0) = \begin{bmatrix} G^{ee}_{\rho\rho} & G^{ee}_{\rho\phi} & G^{ee}_{\rho z} \\ G^{ee}_{\phi\rho} & G^{ee}_{\phi\phi} & G^{ee}_{\phi z} \\ G^{ee}_{z\rho} & G^{ee}_{z\phi} & G^{ee}_{zz} \end{bmatrix}, \tag{17}$$

where $G^{ee}_{\alpha\beta}$ is the component $\alpha = \{\rho, \phi, z\}$ of electric field at the point of observation $\mathbf{r}$ due to an electric point excitation at $\mathbf{r}_0$ with polarization in the $\beta = \{\rho, \phi, z\}$ direction, i.e.,

$$G^{ee}_{\alpha\beta} = \mathbf{E}\big[\mathbf{r};\ \mathbf{J} = \hat{\beta}\delta(\mathbf{r} - \mathbf{r}_0)\big] \cdot \hat{\alpha}. \tag{18}$$

Analogously, the elements for composing other DGFs are given by

$$G^{eh}_{\alpha\beta} = \mathbf{E}\big[\mathbf{r};\ \mathbf{M} = \hat{\beta}\delta(\mathbf{r} - \mathbf{r}_0)\big] \cdot \hat{\alpha}, \tag{19}$$

$$G^{hh}_{\alpha\beta} = \mathbf{H}\big[\mathbf{r};\ \mathbf{M} = \hat{\beta}\delta(\mathbf{r} - \mathbf{r}_0)\big] \cdot \hat{\alpha}, \tag{20}$$

$$G^{he}_{\alpha\beta} = \mathbf{H}\big[\mathbf{r};\ \mathbf{J} = \hat{\beta}\delta(\mathbf{r} - \mathbf{r}_0)\big] \cdot \hat{\alpha}. \tag{21}$$

The pseudo-analytic axial mode-matching formulation presented in [7] [36, Ch. 3] will be refashioned in what follows for allowing the extraction of the DGF elements demanded in (18)–(21). We can express the DGF coefficients as a modal sum of azimuthal (n) and radial (p) harmonics according to

$$G^{ee}_{\alpha\beta} = \sum_{n=-N}^{N} \sum_{p=1}^{P} (A^{e+}_{r,np,\beta} + A^{e-}_{r,np,\beta})\, e_{\alpha,np}(\rho)\, e^{in\phi}, \tag{22}$$

$$G^{eh}_{\alpha\beta} = \sum_{n=-N}^{N} \sum_{p=1}^{P} (A^{h+}_{r,np,\beta} + A^{h-}_{r,np,\beta})\, e_{\alpha,np}(\rho)\, e^{in\phi}, \tag{23}$$

$$G^{hh}_{\alpha\beta} = \sum_{n=-N}^{N} \sum_{p=1}^{P} (A^{h+}_{r,np,\beta} - A^{h-}_{r,np,\beta})\, h_{\alpha,np}(\rho)\, e^{in\phi}, \tag{24}$$

$$G^{he}_{\alpha\beta} = \sum_{n=-N}^{N} \sum_{p=1}^{P} (A^{e+}_{r,np,\beta} - A^{e-}_{r,np,\beta})\, h_{\alpha,np}(\rho)\, e^{in\phi}, \tag{25}$$

for $\alpha = \{\rho, \phi\}$, and

$$G^{ee}_{z\beta} = \sum_{n=-N}^{N} \sum_{p=1}^{P} (A^{e+}_{r,np,\beta} - A^{e-}_{r,np,\beta})\, e_{z,np}(\rho)\, e^{in\phi}, \tag{26}$$

$$G^{eh}_{z\beta} = \sum_{n=-N}^{N} \sum_{p=1}^{P} (A^{h+}_{r,np,\beta} - A^{h-}_{r,np,\beta})\, e_{z,np}(\rho)\, e^{in\phi}, \tag{27}$$

$$G^{hh}_{z\beta} = \sum_{n=-N}^{N} \sum_{p=1}^{P} (A^{h+}_{r,np,\beta} + A^{h-}_{r,np,\beta})\, h_{z,np}(\rho)\, e^{in\phi}, \tag{28}$$

$$G^{he}_{z\beta} = \sum_{n=-N}^{N} \sum_{p=1}^{P} (A^{e+}_{r,np,\beta} + A^{e-}_{r,np,\beta})\, h_{z,np}(\rho)\, e^{in\phi}, \tag{29}$$

where $e_{\alpha,np}(\rho)$ and $h_{\alpha,np}(\rho)$ are the ρ-dependent parcels of the electric and magnetic fields, respectively, $\exp(in\phi)$ is displaying its ϕ-dependence, and the z-dependence is embedded into $A^{f\pm}_{r,np,\beta}$, with $f = \{e, h\}$. Further details can be found in [7].

All the np modal coefficients $A^{f\pm}_{r,np,\beta}$ can be written into the column vectors $\bar{A}^{f\pm}_{r,\beta}$. These vector represents forward and backward propagating amplitudes at the observation place z due to an elementary electric or magnetic dipole sources, for $f = e$ and $f = h$, respectively. We can also write column vectors combining the source excitation amplitudes as $\bar{A}^{f\pm}_{r_0,\beta}$.

The modal source excitation is given by

$$A^{f\pm}_{r_0,np,\beta} = \frac{S^{f\pm}_{np,\beta}}{N_{np}}, \tag{30}$$

where

$$S^{e\pm}_{np,\beta} = S^{\pm}_{np}[\mathbf{J} = \hat{\beta}\delta(\mathbf{r} - \mathbf{r}_0);\ \mathbf{M} = \mathbf{0}], \tag{31}$$

$$S^{h\pm}_{np,\beta} = S^{\pm}_{np}[\mathbf{J} = \mathbf{0};\ \mathbf{M} = \hat{\beta}\delta(\mathbf{r} - \mathbf{r}_0)], \tag{32}$$

with [36, eq. (3-225)]

$$\begin{aligned} S^{\pm}_{np}[\mathbf{J};\mathbf{M}] &= (-1)^n \int_V \Big[(-s_n e_{\rho,np}\hat{\rho} + e_{\phi,np}\hat{\phi} \pm s_n e_{z,np}\hat{z}) \cdot \mathbf{J} \\ &\quad \pm (h_{\rho,np}\hat{\rho} - s_n h_{\phi,np}\hat{\phi} \mp h_{z,np}\hat{z}) \cdot \mathbf{M}\Big] \\ &\quad \times e^{-in\phi} e^{\mp ik_{z,np}z}\, dv, \end{aligned} \tag{33}$$

$$N_{np} = 4\pi(-1)^n \int (s_n e_{\rho,np} h_{\phi,np} + e_{\phi,np} h_{\rho,np})\rho\, d\rho. \tag{34}$$

where $s_n = 1 - 2\delta_{0,n}$, with the Kronecker delta $\delta_{0,n}$ returning 1 if $n = 0$, and 0 otherwise. In the above, the ρ-dependence of the fields was omitted for simplicity. Closed-form solution is well-known for N_{np} [7]. The space-impulsive nature of the elementary sources $\mathbf{J}$ and $\mathbf{M}$ required in (31) and (32) allows us to easily found closed-form expressions for (30). Now, we can finally assembly the associated source coefficients $\bar{A}^{f\pm}_{r_0,\beta}$, at $z = z_0$ and combine them with the generalized scattering matrices introduced in [36, Appendix B] for obtaining $\bar{A}^{f\pm}_{r,\beta}$, i.e., the amplitudes at the observation plane z required in DGF elements in (22)–(29). The details are presented in [7], [36], where closed-form generalized reflection and transmission matrices where obtained via a mode-matching technique.

D. VOLTAGE AT THE RX SENSOR

The well-logging tools used today [1], [2] employ horizontal- and tilted-coil antennas as receiving sensor, and the induced voltage (electromotive force) at such RXs is the main output parameter of interest for the geophysical prospecting. This voltage can be obtained by integrating the total electric field due to the impressed and equivalent sources ($\mathbf{E}_b + \mathbf{E}_s$) along the coil path, i.e.,

$$V_{RX} = -\int_V \mathbf{E}(\mathbf{r}) \cdot \boldsymbol{\delta}_R\, dv, \tag{35}$$

where

$$\begin{aligned} \boldsymbol{\delta}_R &= \delta(\rho - \rho_R) \\ &\quad \times \delta[z - z_R + \rho_R \tan(\theta_R)\, \cos(\phi - \phi_R)] \\ &\quad \times [\hat{\phi} + \hat{z} \tan(\theta_R)\, \sin(\phi - \phi_R)]. \end{aligned} \tag{36}$$

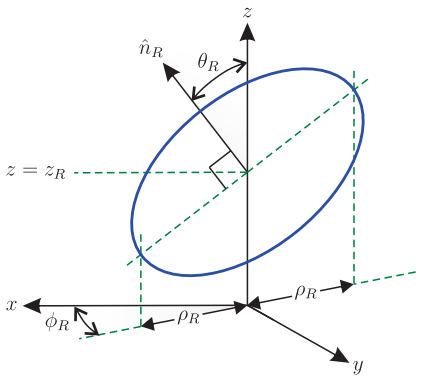

FIGURE 2. Geometry of a tilted-coil antenna.

where $\delta(\cdot)$ is the Dirac delta, ρ_R and z_R are the radial and longitudinal positions of the center of the tilted-coil antenna, and ϕ_R and θ_R are the azimuthal and elevation tilt angles [37], as depicted in Fig. 2. The integral associated with the background field contribution can be computed analytically [7, eqs. (51)–(56)], whereas the parcel for the scattered field can be computed numerically via a line integral along the RX antenna perimeter.

III. NUMERICAL RESULTS

In what follows, we consider an idealized LWD sensor consisting of one TX and one RX coil antennas inside a borehole. The antennas are concentrically wrapped around a perfect electric conducting mandrel. The radii of the mandrel and coil antennas are 4-in and 4.5-in, respectively (where 1 in $=$ 0.0254 m). In all cases we have explored, the TX operates at 2 MHz, by carrying a 1 A current. We will now explore the ability of the presented method for computing the LWD sensor response (i.e., the induced voltage at RX) for scenarios where an axi-symmetric well is perturbed by an object outside the borehole.

A. ISOTROPIC AND SYMMETRIC INVASION

We consider first an isotropic geophysical formation comprising a cylindrically layered background with two horizontal and two vertical layers, as depicted in Fig. 1. A 5-in-radius borehole is filled with oil-based mud characterized by the electric conductivity $\sigma = 5 \times 10^{-4}$ S/m, while formations 1 and 2 have $\sigma = 5$ S/m and $\sigma = 1$ S/m, respectively. All layers have relative permittivity $\epsilon_r = 1$ and relative permeability $\mu_r = 1$. In addition, formation 2 is invaded by an isotropic and axi-symmetric layer having σ_s, with radial and longitudinal thickness $d = 10$ in and $h = 10$ in, respectively. See Fig. 1 with $\alpha = 2\pi$. The LWD sensor comprises horizontal-coil antennas that move axially through the extension of the well, and as a reference, the longitudinal positions of the TX and RX are $z = z_T$ and $z = z_T + 30$ in, respectively. Figs. 3 and 4 show the voltage at RX as a function of the axial position z_T, considering several values of σ_s, from 0.1 S/m to 5 S/m. Good agreement is observed

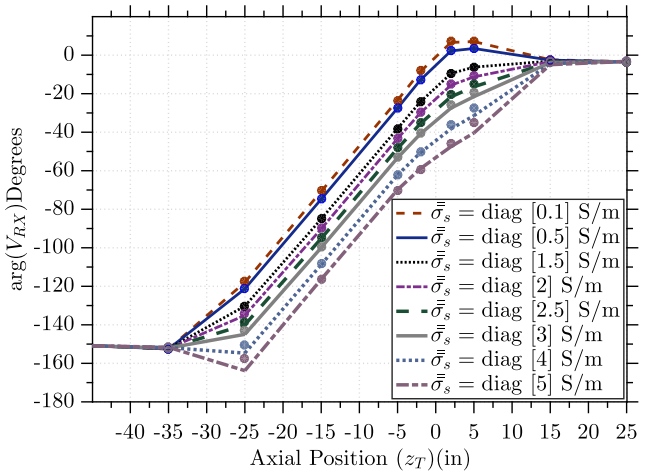

FIGURE 3. Phase of the voltage at RX for several values of conductivity σ_s. Solid lines show results obtained by the BA-based method, whereas the small symbols denote mode-matching-based results from the method presented in [36].

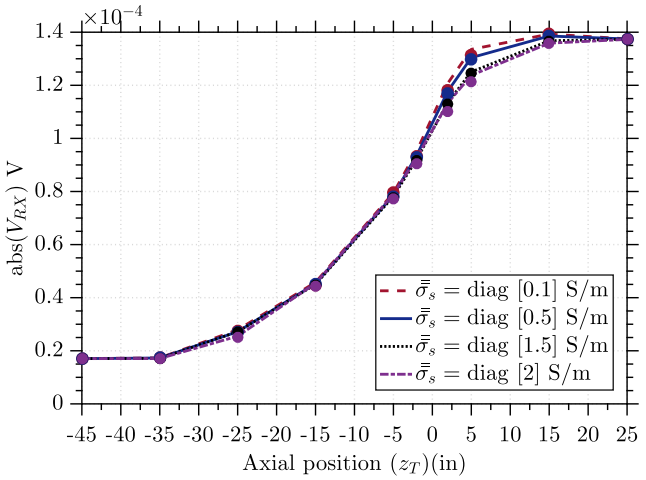

FIGURE 4. Amplitude of the voltage at RX for several values of conductivity σ_s. Solid lines show results obtained by the BA-based method, whereas the small symbols denote mode-matching-based results from the method presented in [36].

versus the analitical results from the mode-matching-based method presented in [36].

The mode-matching method alone allows us to model this symmetric-invasion problem. We used here the BA for evaluating the invasion-zone effects using the mode-matching solution only for computing the background field contributions. Notice that only the azimuthal harmonic associated with $n = 0$ is required for computing the received voltage because of the symmetric characteristics of excitation and the media.

Fig. 3 shows that the electrical conductivity of the invaded-zone σ_s affects significantly the phase of the voltage at RX. On other hand, the invasion zone does not disturb with the same intensity the amplitude of the induced voltage. A manifestation of the restraints that BA in (13) and (14) renders to the present method is the increase in the error on the computed voltage that becomes apparent when $\sigma_s > 1.5$ S/m.

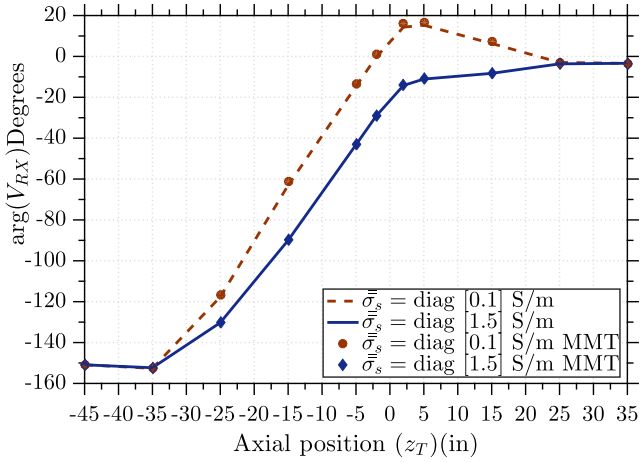

FIGURE 5. Phase of the voltage at RX due to a symmetric invasion with $h = 20$ in.

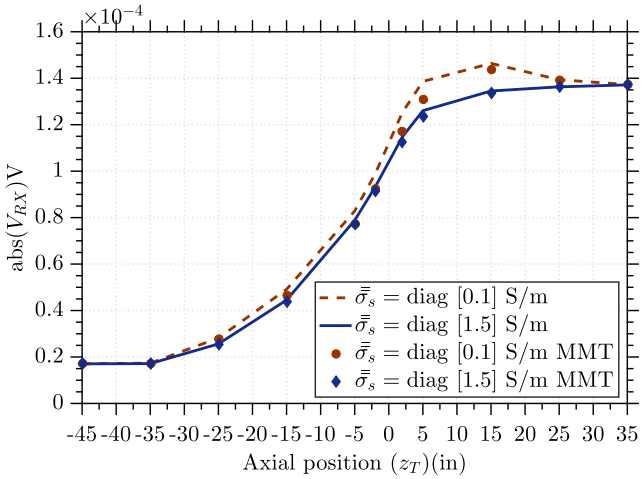

FIGURE 6. Amplitude of the voltage at RX due to a symmetric invasion with $h = 20$ in.

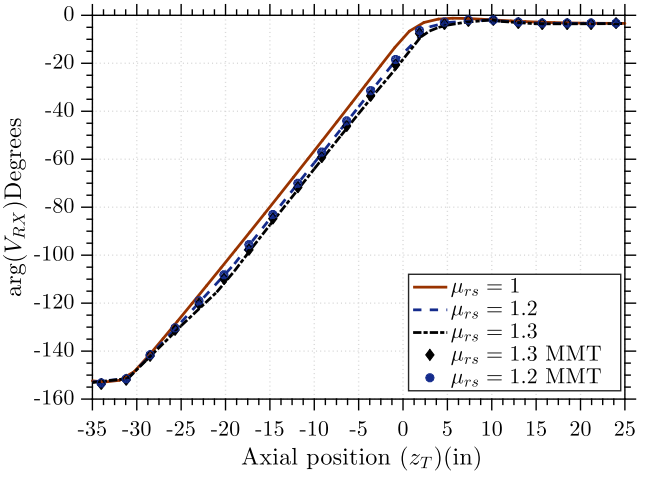

FIGURE 7. Phase of the voltage at RX due to magnetic permeability variations.

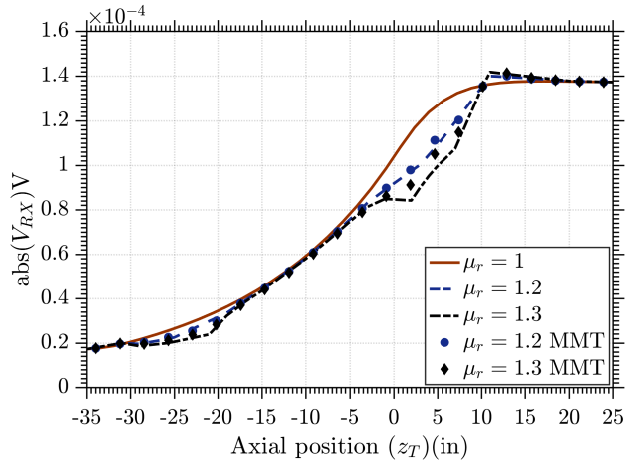

FIGURE 8. Amplitude of the voltage at RX due to magnetic permeability variations.

To further investigate the ability of the present approach for assessing the effects of a ticker invasion-zone, we consider now that $h = 20$ in, while keeping all other parameters as before. Figs. 5 and 6 show the voltage at RX for the cases where the invasion-zone has $\sigma_s = 0.1$ S/m and $\sigma = 1.5$ S/m. Even doubling the invasion-zone longitudinal thickness, we obtained relatively accurate voltage results. A slight deviation between the reference (mode-matching-based) and the presented perturbational method was observed on the voltage amplitude when $\sigma_s = 0.1$ S/m. Such deviations are not relevant when $\sigma_s = 1.5$ S/m because the BA corrections are proportional to $\Delta\epsilon$ and $\Delta\mu$ as seen in (15) and (16).

As an additional test, we consider now that the symmetric invasion zone has the relative magnetic permeability μ_{rs}, and the conductivity $\sigma_s = 1$ S/m, again with $d = 10$ in and $h = 10$ in. Fig. 7 and Fig. 8 show the voltage at RX computed via the mode-matching technique and via the present BA approach for two cases: $\mu_{rs} = 1.2$ and $\mu_{rs} = 1.3$. As before, we observe a good agreement between the models. The amplitude of the voltage is sensitive to the magnetic constitutive parameters of the scatterer, since a variation of 20% in the permeability of the background media implies a vast change of the sensor response, with the occurrence of horn effects. The BA approach diverges from the reference solution as μ_{rs} increases.

B. ANISOTROPIC AND SYMMETRIC INVASION

We next consider a formation similar to the latter problem, but with an anisotropic invasion zone. For validation purposes, we consider two invasion uniaxial materials filling the scattering object, described by the conductivity tensors $\bar{\bar{\sigma}}_s = \text{diag}\,[0.5, 0.5, 2]$ S/m and $\bar{\bar{\sigma}}_s = \text{diag}\,[2, 2, 0.5]$ S/m. Figs. 9 and 10 plot the amplitude and phase of the voltages at RX as the sensor moves longitudinally. Good agreement is observed in the BA-based results of the method proposed here versus the mode-matching-based ones from the method presented in [36]. Additionally, we consider a biaxial material with $\bar{\bar{\sigma}}_s = \text{diag}\,[0.5, 1.5, 2]$ S/m, i.e., a

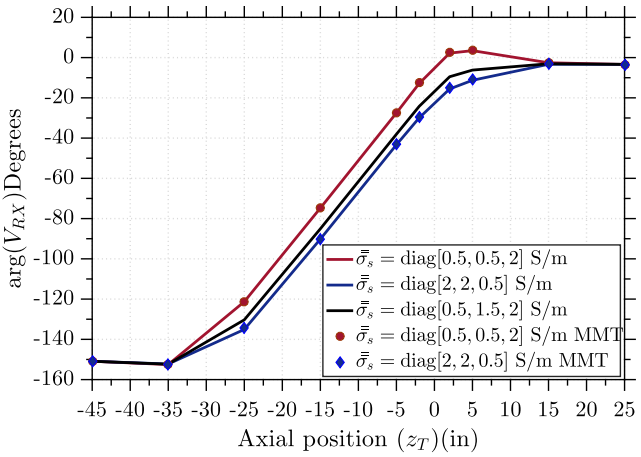

FIGURE 9. Phase of the voltage at RX due to anisotropic symmetric invasion zones.

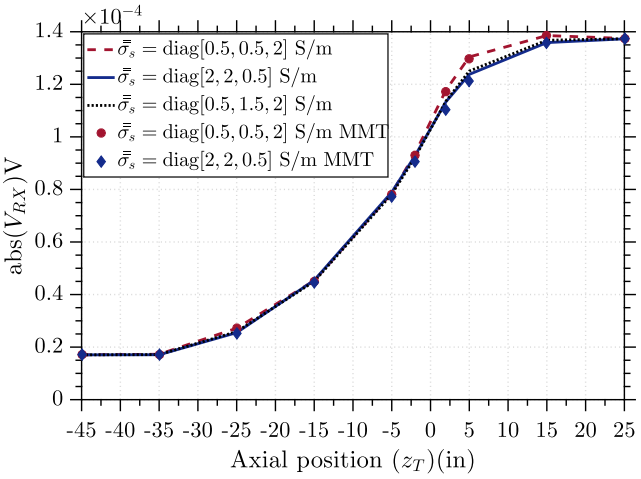

FIGURE 10. Amplitude of the voltage at RX due to anisotropic symmetric invasion zones.

conductivity slightly different from uniaxial scenarios. The pseudo-analytical mode-matching method in [36] cannot solve this biaxial media problem, but it can be combined with the perturbation approach described in Section II for rendering the receiving voltage results depicted in Figs. 9 and 10. Physically meaningful results are observed.

C. NON-SYMMETRIC INVASION

Consider now the non-symmetric invasion zone depicted in Fig. 1, where the scattering object has $\sigma = 2$ S/m and spans over the cylindrical sector defined by 5 in $\leq \rho \leq$ (5 in $+ d$), $0 \leq \phi \leq \alpha$, and $0 \leq z \leq h$, with $d = 10$ in, and $h = 10$ in. All other parameters are kept as in the case explored in Section III-A, where horizontal-coil antennas are employed as a LWD sensor. Figs. 11 and 12 show phase and amplitude of the received voltage at RX for three invasion cases: $\alpha = \{0°, 180°, 360°\}$. For $\alpha = 0°$ there is no invasion anymore, and the total voltage is the background field alone, i.e., $\mathbf{E}_s = \mathbf{0}$. For $\alpha = 360°$, the problem becomes symmetric again, but now we have $\mathbf{E}_s \neq \mathbf{0}$. For $\alpha = 180°$, the scatterer is asymmetrical, and, consequently, we need to compute $\mathbf{E}_s$ as a sum of modal fields due to the azimuthal harmonics with $n = \{0, -1, 1, -2, +2, \dots\}$. For the $\alpha = 0°$ and $\alpha = 360°$ scenarios, in contrast, we only need to consider fields associated with $n = 0$. In all cases, the background field $\mathbf{E}_b$ requires only azimuthal variations associated with $n = 0$ because of the horizontal-coil TX excites only transverse electric (TE^z) fields [7], [37]. The voltage results of the cases with $\alpha = 0°$ and $\alpha = 360°$ where validated before in Section III-A. For the case with $\alpha = 180°$, the convergence of the present method was observed using $n = \{0, -1, 1\}$. It is important to stress that our perturbation solution predicts plausible receiving voltages in the case $\alpha = 180°$ if compared with the extreme scenarios $\alpha = \{0°, 360°\}$.

Figs. 11 and 12 also present results from finite-integration technique (FIT) solver from CST Studio Suite [38] for the non-axisymmetric scenario $\alpha = 180°$. Good agreement is observed versus the presented BA-based method. To avoid very long simulation times on simulating the original structure in the 3D-FIT solver, the problem was considered in CST using a scale factor of 10. Namely, the excitation frequency and the electrical conductivity were multiplied by 10, while the spatial dimensions were divided by 10. This scaled model required 18865080 mesh cells until convergence and the CPU time required for each point of simulation (shown in Figs. 11 and 12) was 7 h, 6 m, 19 s, requiring about 2.756 GB of memory, when using a dedicated Workstation with a 2.10-GHz Intel Xeon E5-2620 v2 12-core processor. On the other hand, the computational cost for each simulation point in our Fortran 90 implementation of the presented method was about 2 minutes of CPU time and about 25 MB of memory.

Simulations times, we simulate a radially bounded structure, using a radial domain truncated by a PEC layer at $=$ 10 in. To avoid further enlargement of the computational domain,

The $\alpha = 180°$ case was validated comparing our method with the time-domain solver of CST STUDIO SUITE, good agreement was obtained.

It is important to stress that due to the long simulation time required in a 3D time-domain method, the problem was simulated in CST using a scale factor of ten. That is, the frequency and conductivity were multiplied by ten while the dimensions were divided by ten. Even in the scaled model, to get the results for each point showed in Figs. 11 or 12, the required computational time was long. Each simulation required approximately 20×10^6 mesh cells to get convergence, and it takes approximately 7 hours. On the other hand, our implementation takes about 2 minutes for each point, and it is possible to execute all the points simultaneously

D. ANISOTROPIC DIPPING LAYER

Next, consider that the LWD sensor is traveling a layered earth formation with a dipping bed, as depicted in Fig. 13. This layer has a vertical thickness $h = 10$ in, and is filled with a uniaxial anisotropic and homogeneous material characterized by the conductivity tensor $\bar{\bar{\sigma}}_s = \text{diag}\,[1.2, 1.2, 0.8]$ S/m,

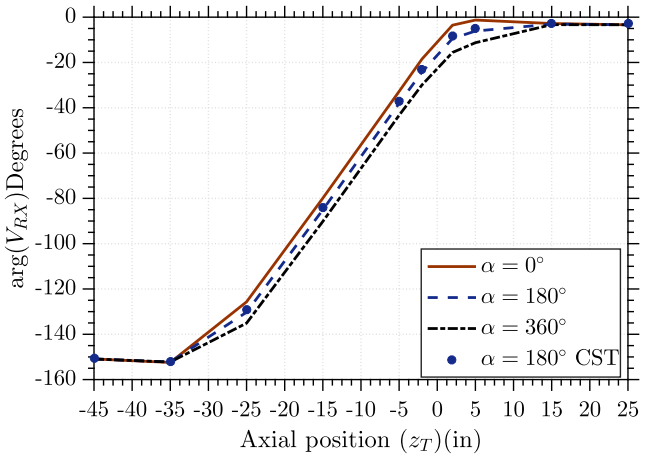

FIGURE 11. Phase of the voltage at RX due to an invasion-zone defined by the azimuthal angle α. Results obtained by the BA-based method are shown by lines, whereas the small dots denote FIT results from [38].

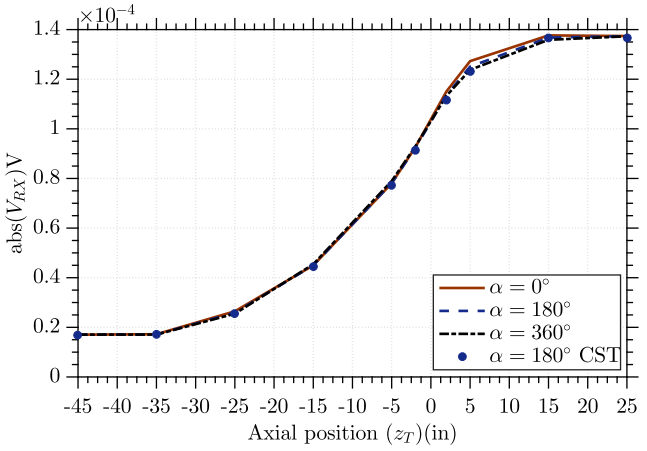

FIGURE 12. Amplitude of the voltage at RX due to an invasion-zone defined by the azimuthal angle α. Results obtained by the BA-based method are shown by lines, whereas the small dots denote FIT results from [38].

defined in respect to the global cylindrical coordinate system (ρ, ϕ, z). This layer is now tilted according to the dipping angle θ_s, as shown in Fig. 13. For this hypothetical scenario, we consider a uniaxial background formation having $\bar{\bar{\sigma}}_b = \text{diag}\,[1, 1, 0.5]$ S/m, and an isotropic borehole with $\sigma = 2$ S/m. Again, the TX and RX are horizontal-coil antennas, now placed at z_T and $z = z_T + 24$ in, respectively. All other simulation parameters are kept as in the case explored in Section III-A.

Fig. 14 shows the phase of the voltage measured by the RX as a function of the axial position z_T for five dipping angles: $\theta_s = \{0°, 30°, 50°, 60°, 70°\}$. We stress that the vertical thickness h and the conductivity tensor $\bar{\bar{\sigma}}_s$ are the same for all the investigated dipping angles θ_s. The results obtained again show good agreement with those from [36] in case of $\theta_s = 0°$. Comparing the simulated results, we can observe that the apparent thickness of the dipping bed increases with the dipping angle as a consequence of a slower equivalent

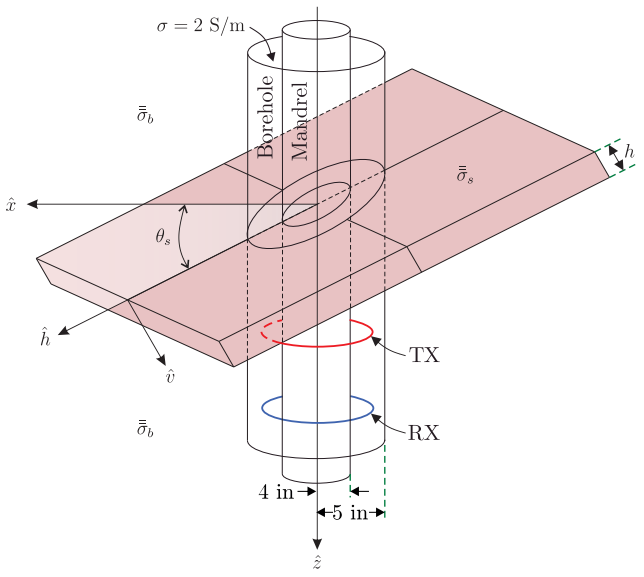

FIGURE 13. Well-logging tool traversing a dipping bed layer.

conductivity transition this geometry provided. This is in consonance with the shoulder-bed effects identified in [11].

A more realistic geophysical scenario considers the dipping-bed layer as a uniaxial anisotropic media, but in respect to its *local* coordinate system, e.g., the $\bar{\bar{\sigma}}_s = \text{diag}[\sigma_h, \sigma_h, \sigma_v]$ expressed in terms of the electrical conductivities in the horizontal (σ_h) and vertical (σ_v) directions of the dipping bed. In terms of the *global* cylindrical coordinate system (ρ, ϕ, z), the conductivity tensor of the scatterer is transformed into [11], [24]

$$\bar{\bar{\sigma}}_s = \begin{bmatrix} \sigma^s_{\rho\rho} & \sigma^s_{\rho\phi} & \sigma^s_{\rho z} \\ \sigma^s_{\phi\rho} & \sigma^s_{\phi\phi} & \sigma^s_{\phi z} \\ \sigma^s_{z\rho} & \sigma^s_{z\phi} & \sigma^s_{zz} \end{bmatrix}, \tag{37}$$

where

$$\sigma^s_{\rho\rho} = \sigma_\rho \cos^2\phi + \sigma_\phi \sin^2\phi, \tag{38}$$
$$\sigma^s_{\rho\phi} = -\sigma_\rho \sin\phi\cos\phi + \sigma_\phi \sin\phi\cos\phi, \tag{39}$$
$$\sigma^s_{\rho z} = (\sigma_v - \sigma_h)\cos\phi\sin\theta_s\cos\theta_s, \tag{40}$$
$$\sigma^s_{\phi\rho} = -\sigma_\rho \cos\phi\sin\phi + \sigma_\phi \sin\phi\cos\phi, \tag{41}$$
$$\sigma^s_{\phi\phi} = \sigma_\rho \sin^2\phi + \sigma_\phi \cos^2\phi, \tag{42}$$
$$\sigma^s_{\phi z} = -(\sigma_v - \sigma_h)\sin\phi\sin\theta_s\cos\theta_s, \tag{43}$$
$$\sigma^s_{z\rho} = (\sigma_v - \sigma_h)\cos\phi\sin\theta_s\cos\theta_s, \tag{44}$$
$$\sigma^s_{z\phi} = -(\sigma_v - \sigma_h)\sin\phi\sin\theta_s\cos\theta_s, \tag{45}$$
$$\sigma^s_{zz} = \sigma_h \sin^2\theta_s + \sigma_v \cos^2\theta_s, \tag{46}$$
$$\sigma_\rho = \sigma_h \cos^2\theta_s + \sigma_v \sin^2\theta_s, \tag{47}$$
$$\sigma_\phi = \sigma_h. \tag{48}$$

Fig. 15 shows the phase response of the LWD sensor traversing an anisotropic dipping-bed layer with the dipping angle $\theta_s = 30°$, for four conductivity scenarios:

- With the full tensor $\bar{\bar{\sigma}}_{s1}$, determined by using $\sigma_h = 1.2$ S/m and $\sigma_v = 0.8$ S/m into (37),

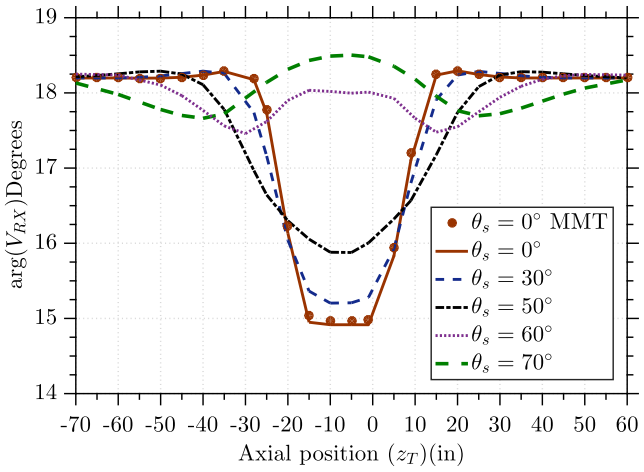

FIGURE 14. Phase of the voltage at RX due to a LWD sensor traversing a dipping bed.

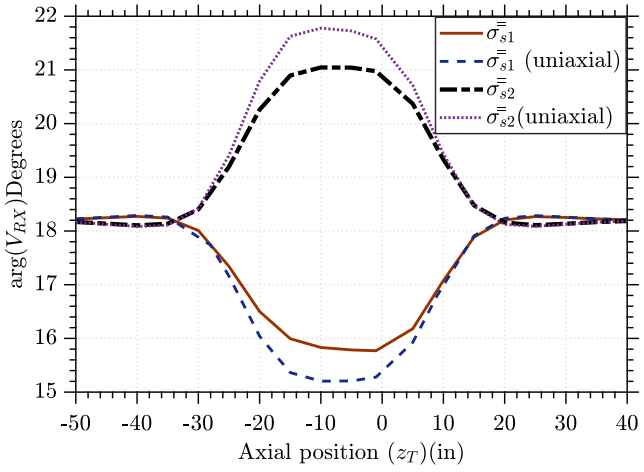

FIGURE 15. Phase of the voltage at RX due to a LWD sensor traversing an anisotropic dipping bed.

- With the full tensor $\bar{\bar{\sigma}}_{s2}$, determined by using $\sigma_h = 0.8$ S/m and $\sigma_v = 0.3$ S/m into (37),
- With the uniaxial tensor $\bar{\bar{\sigma}}_{s1}$(uniaxial) = diag[1.2, 1.2, 0.8], and,
- With the uniaxial tensor $\bar{\bar{\sigma}}_{s2}$(uniaxial) = diag[0.8, 0.8, 0.3].

We can observe the effects of the fully anisotropic tensor in (37) on the RX voltage versus the uniaxial counterparts.

E. BOREHOLE FAILURE

The heterogeneity of formation materials may cause borehole failures, eventually resulting in a shaped damage zone around the circular borehole [39]. To explore such failure effects on the LWD response, consider now a sensor traversing a background formation with $\sigma = 1$ S/m. Again, the radii of the mandrel and coil antennas are 4-in and 4.5-in, respectively. Water-based mud with $\sigma = 2$ S/m is used as a drilling fluid in the borehole. An elliptical-shaped borehole deformation is considered over the longitudinal section $0 < z < h$, with

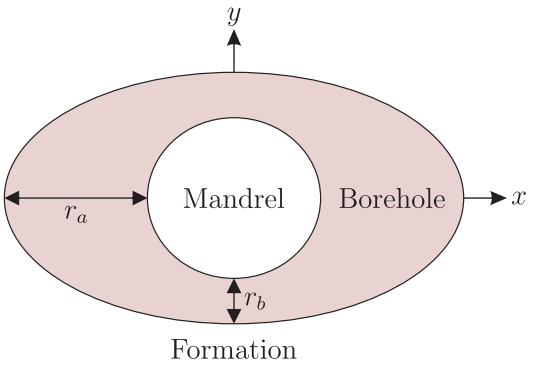

FIGURE 16. Oval-shaped borehole.

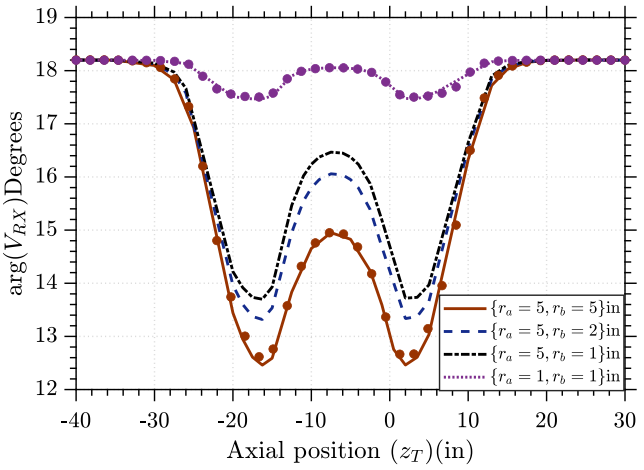

FIGURE 17. Phase of the voltage at RX due to a LWD sensor traversing an oval-shaped borehole having a thickness of $h = 10$ in. Results obtained by the BA-based method are shown by lines, whereas the small symbols denote mode-matching-based results from the method presented in [36].

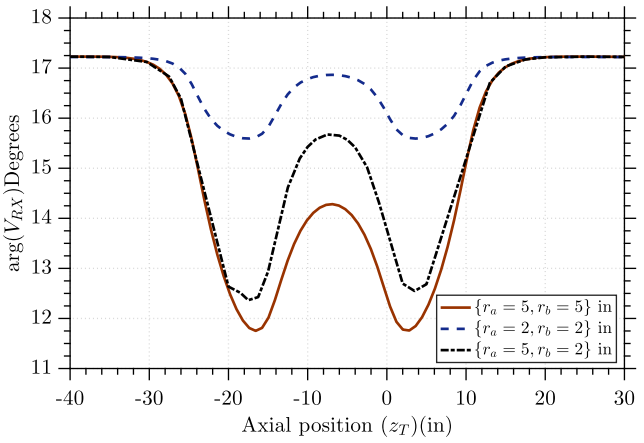

FIGURE 18. Phase of the voltage at a tilted-coil RX due to a LWD sensor traversing an oval-shaped borehole having a longitudinal thickness of $h = 10$ in.

$h = 10$ in. The thickness r_a in and r_b in are used to define the borehole, as depicted in Fig. 16, conforming to the radial boundary

$$\rho_{ell}(\phi) = \frac{(4 + r_a)(4 + r_b)}{[(4 + r_b)\cos(\phi)]^2 + [(4 + r_a)\sin(\phi)]^2}, \quad (49)$$

computed in inches. Outside this failure domain, over the longitudinal sections $z < 0$ and $z > h$, we have an ordinary 5-in-radius circular borehole.

Fig. 17 shows the phase of the voltage measured by a horizontal-coil RX (placed at $z = z_T + 24$ in) as a function of the axial position z_T, for different values of r_a and r_b. In case of $r_a = r_b$, we compare the results of the present BA-based solution versus the mode-matching method in [36]. In the borehole failure scenarios with $r_a = 5$ in and $r_b = 2$ in, and $r_a = 5$ in and $r_b = 1$ in, we can observe the effects of a non-circular invasion zone on the RX voltage curves.

Finally, we consider the same case explored above, but now using a LWD sensor with tilted-coil antennas: the transmitter and receiver tilt angles are $\theta_T = 10°$ and $\theta_R = 10°$, respectively. Fig. 18 shows the phase of the voltage as a function of the axial position z_T for several different values of r_a and r_b. Convergence was observed on computing $\mathbf{E}_b$ and $\mathbf{E}_s$ using the azimuthal harmonics $n = \{0, -1, 1\}$. The contribution of the other high-order harmonics is negligible. Notice that the $\mathbf{E}_b$ field due to the tilted-coil TX excites TE^z modes associated with $n = 0$, and hybrid modes (linear combination of TE^z and TM^z) associated with $n = \{-1, 1\}$. There is no TM^z field with $n = 0$ excited by such kind of source [36]. For completeness, $\mathbf{E}_s$ includes contributions of both TE^z and TM^z with $n = 0$ as well as hybrid modes with $n = \{-1, 1\}$.

IV. CONCLUSION

In this work, we introduced a perturbational formulation to model electromagnetic well-logging sensors in complex anisotropic formations. A mode-matching technique was used for computing the DGFs in cylindrically stratified media, and then a Born approximation was used to evaluate the effects of non-symmetric borehole environments on the LWD sensor response. The computational cost of the numerical algorithms developed in this work is relatively low if compared to that required in brute-force techniques such as finite elements, finite differences, and method of moments. Our approach requires only a volumetric integral over the non-axisymmetric region instead of a numerically expensive integral over the entire domain, as in the standard BA implementation. The proposed perturbation method can accurately model LWD sensors when the borehole is disturbed by small scatterers with constitutive parameters slightly different from those of the background media. Under other conditions, brute-force numerical methods are recommended. As future work, we plan to evaluate the limitations of the perturbational method proposed here in terms of the BA theory, i.e., the scatterer size and the abrupt variations of the profile of σ and μ.

REFERENCES

[1] *ADR Azimuthal Deep Resistivity Sensor Datasheet*, Halliburton Sperry Drilling, Houston, TX, USA, 2016.

[2] *EarthStar Ultra-Deep Resistivity Service Datasheet*, Halliburton Sperry Drilling, Houston, TX, USA, 2018.

[3] *EarthStar Ultra-Deep Resistivity Service*, Weatherford, Houston, TX, USA, 2018.

[4] *Oilfield Technology MLWD QA*, Halliburton, Houston, TX, USA, 2017.

[5] *EarthStar Ultra-Deep Resistivity Service*, Halliburton, Houston, TX, USA, 2018.

[6] *AFR Azimuthal Focused Resistivity Sensor*, Halliburton, Houston, TX, USA, 2016.

[7] G. S. Rosa, J. R. Bergmann, and F. L. Teixeira, "A robust mode-matching algorithm for the analysis of triaxial well-logging tools in anisotropic geophysical formations," *IEEE Trans. Geosci. Remote Sens.*, vol. 55, no. 5, pp. 2534–2545, May 2017.

[8] Y. Li, X. Sun, G. Su, M. Wang, and R. Li, "Numerical simulation and analysis of multicomponent induction logging response in anisotropic formation," *IEEE Access*, vol. 8, pp. 149345–149361, 2020.

[9] J. Wang, J. Li, Y. Chen, F. Han, and Q. H. Liu, "Simulation of 3-D electromagnetic scattering and inverse scattering by arbitrary anisotropic dielectric objects embedded in layered arbitrary anisotropic media," *IEEE Trans. Antennas Propag.*, vol. 68, no. 8, pp. 6473–6478, Aug. 2020.

[10] H. Wang, W.-F. Huang, Y. Fang, R. Zhang, D. Wang, Q. Zhan, and Q. H. Liu, "Efficient and accurate electromagnetic modeling of triaxial induction responses from multiscale fractures for well-logging applications," *IEEE J. Multiscale Multiphys. Comput. Techn.*, vol. 4, pp. 20–28, Jan. 2019, doi: 10.1109/JMMCT.2019.2892944.

[11] H. O. Lee, F. L. Teixeira, L. E. S. Martin, and M. S. Bittar, "Numerical modeling of eccentered LWD borehole sensors in dipping and fully anisotropic Earth formations," *IEEE Trans. Geosci. Remote Sens.*, vol. 50, no. 3, pp. 727–735, Mar. 2012.

[12] L. Zhong, J. Li, A. Bhardwaj, L. C. Shen, and R. C. Liu, "Computation of triaxial induction logging tools in layered anisotropic dipping formations," *IEEE Trans. Geosci. Remote Sens.*, vol. 46, no. 4, pp. 1148–1163, Apr. 2008.

[13] Z. Nie, Z. Liu, and X. Sun, "A multirelay cooperation method for wireless transmission of MWD and LWD signals," *IEEE Trans. Geosci. Remote Sens.*, vol. 56, no. 3, pp. 1229–1237, Mar. 2018.

[14] Y. Fang, J. Dai, Q. Zhan, Y. Hu, M. Zhuang, and Q. H. Liu, "A hybrid 3-D electromagnetic method for induction detection of hydraulic fractures through a tilted cased borehole in planar stratified media," *IEEE Trans. Geosci. Remote Sens.*, vol. 57, no. 7, pp. 1–9, Jul. 2019.

[15] G.-S. Liu, F. L. Teixeira, and G.-J. Zhang, "Analysis of directional logging tools in anisotropic and multieccentric cylindrically-layered earth formations," *IEEE Trans. Antennas Propag.*, vol. 60, no. 1, pp. 318–327, Jan. 2012.

[16] G. S. Rosa, J. R. Bergmann, and F. L. Teixeira, "A perturbation method to model electromagnetic well-logging tools in curved boreholes," *IEEE Trans. Geosci. Remote Sens.*, vol. 56, no. 4, pp. 1979–1993, Apr. 2018.

[17] Y.-K. Hue and F. L. Teixeira, "Analysis of tilted-coil eccentric borehole antennas in cylindrical multilayered formations for well-logging applications," *IEEE Trans. Antennas Propag.*, vol. 54, no. 4, pp. 1058–1064, Apr. 2006.

[18] W. C. Chew, *Waves and Fields in Inhomogeneous Media*. New York, NY, USA: Wiley, 1995.

[19] Q. Liu, "Electromagnetic field generated by an off-axis source in a cylindrically layered medium with an arbitrary number of horizontal discontinuities," *Geophysics*, vol. 58, no. 5, pp. 616–625, May 1993.

[20] Y.-K. Hue and F. L. Teixeira, "Numerical mode-matching method for tilted-coil antennas in cylindrically layered anisotropic media with multiple horizontal beds," *IEEE Trans. Geosci. Remote Sens.*, vol. 45, no. 8, pp. 2451–2462, Aug. 2007.

[21] J. Dai and Q. H. Liu, "Efficient computation of electromagnetic waves in anisotropic orthogonal-plano-cylindrically layered media using the improved numerical mode matching (NMM) method," *IEEE Trans. Antennas Propag.*, vol. 63, no. 8, pp. 3569–3578, Aug. 2015.

[22] H. Wang, H. Tao, J. Yao, and Y. Zhang, "Efficient and reliable simulation of multicomponent induction logging response in horizontally stratified inhomogeneous TI formations by numerical mode matching method," *IEEE Trans. Geosci. Remote Sens.*, vol. 50, no. 9, pp. 3383–3395, Sep. 2012.

[23] Y. Fang, J. Dai, Z. Yu, J. Zhou, and Q. H. Liu, "Through-casing hydraulic fracture evaluation by induction logging I: An efficient EM solver for fracture detection," *IEEE Trans. Geosci. Remote Sens.*, vol. 55, no. 2, pp. 1179–1188, Feb. 2017.

[24] H. O. Lee and F. L. Teixeira, "Cylindrical FDTD analysis of LWD tools through anisotropic dipping-layered Earth media," *IEEE Trans. Geosci. Remote Sens.*, vol. 45, no. 2, pp. 383–388, Feb. 2007.

[25] G. Gao and C. Torres-Verdin, "Efficient numerical simulation of axisymmetric electromagnetic induction measurements using a high-order generalized extended born approximation," *IEEE Trans. Geosci. Remote Sens.*, vol. 44, no. 9, pp. 2445–2453, Sep. 2006.
[26] Z. Xiong, "Electromagnetic modeling of 3-D structures by the method of system iteration using integral equations," *Geophysics*, vol. 57, no. 12, pp. 1556–1561, Dec. 1992.
[27] G. Gao, S. Fang, and C. Torres-Verdín, "A new approximation for 3D electromagnetic scattering in the presence of anisotropic conductive media," in *Proc. 3DDMIII Workshop*, Adelaide, SA, Australia, Feb. 2003, pp. 1–10.
[28] K. Yang and A. E. Yilmaz, "FFT-accelerated analysis of scattering from complex dielectrics embedded in uniaxial layered media," *IEEE Geosci. Remote Sens. Lett.*, vol. 10, no. 4, pp. 662–666, Jul. 2013.
[29] T. J. Cui and W. C. Chew, "Fast algorithm for electromagnetic scattering by buried 3-D dielectric objects of large size," *IEEE Trans. Geosci. Remote Sens.*, vol. 37, no. 5, pp. 2597–2608, Sep. 1999.
[30] C. Torres-Verdín and T. M. Habashy, "Rapid numerical simulation of axisymmetric single-well induction data using the extended born approximation," *Radio Sci.*, vol. 36, no. 6, pp. 1287–1306, Nov. 2001.
[31] G. Gao and C. Torres-Verdin, "High-order generalized extended born approximation for electromagnetic scattering," *IEEE Trans. Antennas Propag.*, vol. 54, no. 4, pp. 1243–1256, Apr. 2006.
[32] T. M. Habashy, R. W. Groom, and B. R. Spies, "Beyond the born and Rytov approximations: A nonlinear approach to electromagnetic scattering," *J. Geophys. Res., Solid Earth*, vol. 98, no. B2, pp. 1759–1775, Feb. 1993.
[33] G. S. Rosa, M. S. Canabarro, J. R. Bergmann, and F. L. Teixeira, "A comparison of two numerical mode-matching methodologies for the analysis of inhomogeneous media with radial and vertical stratifications," *IEEE Trans. Antennas Propag.*, vol. 66, no. 12, pp. 7499–7504, Dec. 2018.
[34] R. F. Harrington, *Time-Harmonic Electromagnetic Fields*. New York, NY, USA: McGraw-Hill, 1961.
[35] A. Q. Howard, W. C. Chew, and M. C. Moldoveanu, "A new correction to the born approximation," *IEEE Trans. Geosci. Remote Sens.*, vol. 28, no. 3, pp. 394–399, May 1990.
[36] G. S. Rosa, "Pseudo-analytical modeling for electromagnetic well-logging tools in complex geophysical formations," Ph.D. dissertation, Pontifical Catholic Univ. Rio de Janeiro, Rio de Janeiro, RJ, Brazil, 2017, doi: 10.17771/PUCRio.acad.30559.
[37] T. Hagiwara, E. J. Banning, R. M. Ostermeier, and S. M. Haugland, "Effects of mandrel, borehole, and invasion for tilt-coil antennas," in *Proc. SPE 78th Ann. Tech. Conf. Exhib.*, Denver, CO, USA, Oct. 2003, pp. 1–11, doi: 10.2118/84245-PA.
[38] *CST Studio Suite 2020*, CST AG, Darmstadt, Germany, 2020.
[39] J. X. Liu, W. C. Zhu, J. Liu, J. C. Sheng, B. H. Brady, and C. A. Tang, "Simulation of progressive borehole failure at multi-lateral junctions," *Petroleum Sci. Technol.*, vol. 25, no. 9, pp. 1185–1198, Oct. 2007.

LISSETH SAAVEDRA (Member, IEEE) received the B.S. degree in electronic engineering from the University of Narino, Pasto, Colombia, in 2013, and the M.S. and Ph.D. degrees in electrical engineering from the Pontifical Catholic University of Rio de Janeiro, Brazil, in 2016 and 2021, respectively. Her research interests include synthesis and analysis of antennas and the study of pseudo-analytical techniques for propagation in complex media.

GUILHERME S. ROSA (Member, IEEE) received the B.S. degree in electrical engineering from the Federal University of Santa Maria, Santa Maria, Brazil, in 2011, and the M.S. and Ph.D. degrees in electrical engineering from the Pontifical Catholic University of Rio de Janeiro, Rio de Janeiro, Brazil, in 2013 and 2017, respectively. He is currently an Adjunct Professor with the Center for Telecommunications Studies, Pontifical Catholic University of Rio de Janeiro. His current research interest includes pseudo-analytical techniques for wave scattering modeling in complex media.

JOSÉ R. BERGMANN (Life Senior Member, IEEE) received the degree in electrical engineering from the Universidade Federal do Rio Grande do Sul, Brazil, in 1975, the M.Sc. degree in electrical engineering from the Instituto Militar de Engenharia, Brazil, in 1979, and the Ph.D. degree in electrical engineering from the Queen Mary College, University of London, London, U.K., in 1986. Since 2007, he has been the Vice President for academic affairs of the Catholic University of Rio de Janeiro, Rio de Janeiro, Brazil. He is currently an Associate Professor with the Catholic University of Rio de Janeiro, where he is also the Head of the Antenna Group, Center of the Telecommunications Studies (CETUC). His research interests include numerical modeling, synthesis, and analysis of reflector systems. He was the Vice President and the President of the Brazilian Microwave and Optoelectronics Society (SBMO), from 1996 to 2000.